Second-harmonic generation in conjugated polymer films: A sensitive probe of how bulk polymer crystallinity changes with spin speed

Ian M. Craig,[a)] Christopher J. Tassone, Sarah H. Tolbert,[b)] and Benjamin J. Schwartz[c)]
Department of Chemistry and Biochemistry, UCLA, Los Angeles, California 90095-1569, USA

In this paper, we examine the second-harmonic generation (SHG) from spin-cast films of the conjugated polymer poly(2-methoxy-5-(2′-ethylhexyloxy)*para*-phenylenevinylene) (MEH-PPV). We find that the SHG intensity depends strongly on the speed used to spin cast the films. Two-dimensional grazing incidence x-ray diffraction (XRD) experiments show that the bulk crystallinity of the MEH-PPV films varies in the same way with spin speed as the SHG intensity. This strongly suggests that instead of being interface specific, the second-harmonic signal from conjugated polymer films is dominated by the crystalline domains in the bulk. The nonmonotonic dependence of both the SHG intensity and the degree of MEH-PPV crystallinity results from a competition between the shear forces and the solvent evaporation rate during spin coating, which produces a maximum degree of crystallinity for MEH-PPV films spin cast at around 1400 rpm. We also use XRD to show that thermal annealing produces MEH-PPV films with a single degree of bulk crystallinity, independent of how they were originally cast. This allows us to model the angle- and thickness-dependent SHG from annealed MEH-PPV films with a single polarizability tensor. We find that the SHG from MEH-PPV films fits best to a bulk-allowed electric quadrupole mechanism, consistent with the bulk SHG seen in other π-stacked aromatic molecules. Thus, rather than providing information about conjugated polymer interfaces, SHG can be used as a sensitive probe of the local degree of crystallinity in the bulk of conjugated polymer films. © *2010 American Institute of Physics.* [doi:10.1063/1.3436517]

I. INTRODUCTION

Conjugated polymers are a well studied class of materials due to their ability to act as plastic semiconductors.[1–4] Although they typically have poor electron and hole mobilities relative to traditional inorganic semiconductors such as silicon or gallium arsenide,[5] their easy solution processability, mechanical flexibility, and wide chemical diversity make them very attractive materials for use in disposable electronics,[6] large-area lighting panels,[7,8] light, flexible photovoltaics,[9] and other applications.

Although much is known about the electronic and optical properties of conjugated polymer films, there are many outstanding questions regarding the nature of conjugated polymer interfaces, particularly questions about the polymer/metal interfaces that are crucial to the operation of optoelectronic devices based on these materials. For example, ostensibly symmetric sandwich-structure devices that consist of a metal electrode thermally evaporated onto a substrate, a spin-coated conjugated polymer active layer and a thermally evaporated top electrode made with the same metal, behave as diodes.[10] The fact that two orders of magnitude more current can be injected from the electrode evaporated onto the polymer than from the electrode onto which the polymer was spin cast indicates that understanding and learning to control the nature of conjugated polymer interfaces is critical to op-

timizing devices fabricated from these materials. Surface-specific spectroscopic studies, such as ultraviolet and x-ray photoelectron spectroscopies, have yielded important information on the elemental and local chemical environment at such interfaces,[11–15] but these spectroscopies can be performed only on exposed polymer surfaces that may not be representative of those in working polymer-based optoelectronic devices.

Even-order nonlinear optical (NLO) spectroscopies, such as second-harmonic generation (SHG) and sum frequency generation (SFG), constitute a family of techniques for the nondestructive study of buried interfaces.[16,17] This is because for most centrosymmetric systems, the dipole approximation makes the second-harmonic signal forbidden everywhere but at the symmetry-breaking interface(s).[18–20] Despite the power of these NLO techniques to yield interface-specific information, they have been only sparsely applied to study conjugated polymer films and their interfaces. We are aware of only two studies applying even-order NLO techniques to films of conjugated polymers. The first study looked at the space-charge buildup in polymer light emitting diodes run in forward bias using electric field-induced second harmonic,[21] a technique that is actually not surface-specific. The second study used SFG spectroscopy in an attempt to measure how the average conjugation length of the semiconducting polymer chains at air/polymer and glass/polymer interfaces differed from that in the bulk.[22]

In this paper, we perform a systematic SHG study of films of one of the best-studied conjugated polymers,

a)Present address: USC Department of Chemistry, Los Angeles, CA 90089.
b)Electronic mail: tolbert@chem.ucla.edu.
c)Electronic mail: schwartz@chem.ucla.edu.

poly(2- methoxy-5- (2′-ethylhexyloxy) *p*-phenylenevinylene) (MEH-PPV), whose chemical structure is shown below in Fig. 4(a). MEH-PPV was one of the first conjugated polymers to combine a relatively easy synthetic route with high solubility in a wide range of common laboratory solvents,[23] providing a large number of routes for processing MEH-PPV into thin films for use in devices. We find that rather than providing information about the conjugated polymer interfaces, the second-harmonic signals from MEH-PPV correlate with the degree of crystallinity in the bulk of the film, as measured by low-angle x-ray scattering. Because the SHG signals depend on the bulk polymer morphology, they also depend strongly on the processing conditions used to cast the film: we find that the SHG signals from MEH-PPV films have a particularly pronounced dependence on the speed at which the films were spin cast. As a result, SHG on conjugated polymer films does not appear to provide useful information on the electronic structure of interfaces, but it does provide a sensitive measure of the microscopic degree of crystallinity of the polymer chromophores in a way that the linear optical properties do not.

II. EXPERIMENTAL

The MEH-PPV used in this study was synthesized using the basic method of Neef and Ferraris.[24,25] We modified the published synthesis slightly,[26] halving the concentration of both the bromine monomer and potassium *tert*-butoxide in order to slow the reaction and reduce gellation. We also recrystallized the final product from methylene chloride rather than tetrahydrofuran (see supplementary information[27]). The purity of the polymer was verified using ^{1}H-NMR in deuterated chloroform and characterized using gel permeation chromatography. We also made SHG measurements on films cast from MEH-PPV purchased from American Dye Source (ADS) and obtained similar results, although we found that the poor solubility of the ADS polymer made it impossible to cover the desired range of solution concentrations and film thicknesses.

To prepare films for study by SHG and x-ray diffraction (XRD), MEH-PPV was first dissolved in chlorobenzene and allowed to stir overnight to ensure complete disentanglement of the polymer chains.[28] 1 in. square borosilicate microscope slides were cleaned by immersion in piranha solution (1:1 conc. H_2SO_4:30% aqueous H_2O_2) for ~1 h, followed by rinsing in de-ionized water. They were then sonicated for 5 min each in 18 MΩ Millipore water, electronic grade acetone, and HPLC grade isopropanol. They were immediately dried under a stream of dry argon, placed into a plasma cleaner for 1 h under 300 mTorr dry air. MEH-PPV films were then deposited onto the clean glass substrates via spin coating; all steps in the polymer dissolution and subsequent processing were carried out in the inert atmosphere of a nitrogen dry box. Following spin coating, the MEH-PPV films were placed on a hot plate at 40 °C for several hours to ensure complete removal of residual solvent. Some films were heated at 210 °C for an additional 12 h to study the effects of thermal annealing. The thickness of the films were controlled both by varying the concentration of the initial

solution and the spin speed. Film thicknesses were determined using a profilometer on a subset on the films, which were then correlated with the absorption peak at 337 nm to construct a Beers' law calibration plot in order to interpolate the thickness of the rest of the films.[29]

For the SHG experiments, a 5 W Spectra-Physics Millennia V diode laser was used to pump a mode-locked Spectra-Physics Tsunami Ti:sapphire laser, the output of which consisted of ~120 fs pulses centered at 800 nm at an 87 MHz repetition rate with an average power of ~500 mW. A half-wave plate (HWP) and a Glan-laser polarizer were used to set the incident polarization and beam intensity, and a Schott glass filter (OG600) was used to remove any residual second harmonic generated from the calcite HWP. Approximately 4% of the beam was picked off with a glass microscope cover slip and focused onto either a *z*-cut quartz plate or a KTP (Potassium Titanyl Phosphate) crystal to generate a reference signal for normalizing out laser fluctuations; the remainder of the beam was focused onto one of the MEH-PPV film samples. The film samples were mounted on a rotation stage that allowed the angle of incidence to be varied throughout the experiment without moving the point where the beam impinges on the sample; the rotation stage and sample were enclosed in an air-tight box with CaF_2 windows and flushed with argon to prevent photo-oxidation of the films. The second-harmonic light transmitted through the sample was then recollimated and passed through a second analyzer polarizer. The 400 nm signal and reference beams were filtered with short-pass and notch filters to remove the majority of the 800 nm fundamental beam, and then further filtered with a 400 nm notch filter before impinging on two photomultiplier tubes (Hammamatsu R7056) each connected to a lock-in amplifier (EG&G 5210 and SRS810) synchronized to a 150 Hz optical chopper (SRS540) placed before the initial HWP. Figure 1(a) shows a schematic of the optical setup with the incident angle defined; more details can be found in the accompanying supplementary information.[27]

Two-dimensional (2D) grazing incidence XRD was carried out at the Stanford Synchrotron Radiation Lightsource (SSRL) on beamline 11-3 with a wavelength of 0.9742 Å. In order to evaluate the alignment of crystalline polymer domains within the films, the 2D scattering data was integrated along the *z*- and *x*-axes independently. To ensure that comparisons of the degree of crystallinity were due solely to differences within the samples, the integrated data was normalized by the incident x-ray flux.

III. RESULTS AND DISCUSSION

A. The basic nature of SHG from thin MEH-PPV films

A representative subset of the incident angle-dependent second-harmonic data collected from some of our MEH-PPV films is shown in Fig. 1(b); this figure shows the data for *p*-polarized incident and exigent beams (*p*-polarized incident beams produced no measurable signal for *s*-polarized exit beams). Over the range of film thicknesses that we explored, 20–700 nm, we found that the intensity of the SHG signal generally increased with increasing film thickness, but that
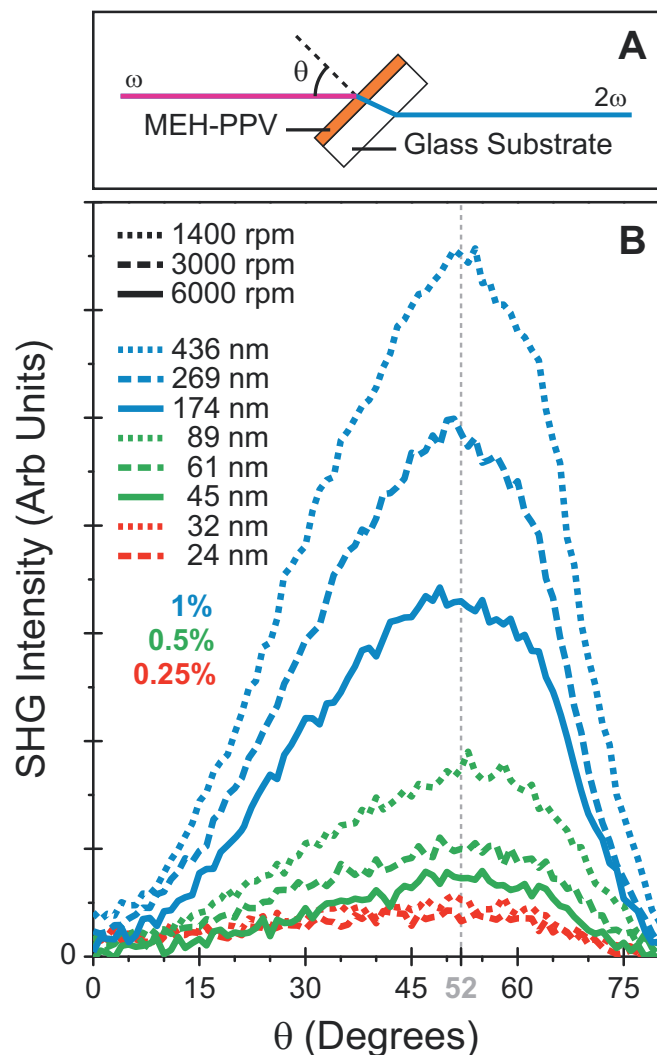
FIG. 1. (a) Schematic of the experimental geometry used for SHG measurements on MEH-PPV films. (b) Angle dependence of the intensity of the second-harmonic light from MEH-PPV films that were spin cast at different spin speeds from chlorobenzene solutions to produce films with different thicknesses; for the data presented, both the 800 nm incident and 400 nm exigent beams were p-polarized. The blue curves denote SHG data taken from MEH-PPV films cast from a 1% w/v solution in chlorobenzene, the green curves correspond to data taken from films cast from a 0.5% w/v solution, and the red curves show the data collected from films cast from a 0.25% w/v solution. Dotted curves show data for films spun at 1400 rpm, dashed curves correspond to films spun at 3000 rpm, and solid curves correspond to films spun at 6000 rpm.
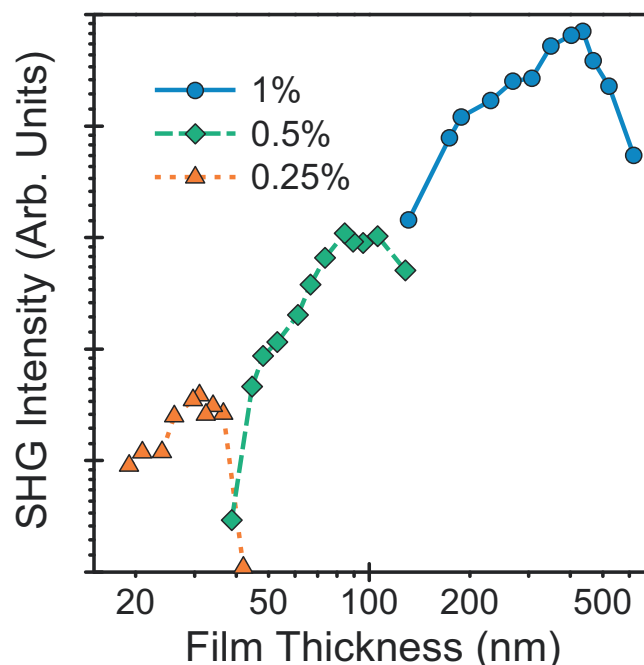

FIG. 2. Angularly integrated SHG data for MEH-PPV films spin cast from solutions with three different concentrations as a function of film thickness; the data are plotted on logarithmic scales on both axes. The orange triangles denote data for films cast from 0.25% w/v MEH-PPV solutions in chlorobenzene, the green diamonds are for films cast from 0.5% w/v solutions, and the blue circles are films cast from 1.0% w/v solutions. Although each set of data shows a general increase in signal intensity with increasing film thickness, the data for the thickest films cast from each solution show a decrease in SHG intensity with increasing film thickness.

the angle dependence changed very little with thickness. The lack of a change of the angle dependence of the SHG with film thickness is somewhat surprising given the large birefringence of MEH films.[30] This is because as the incident angle is varied, the SHG intensity usually exhibits several minima and maxima, known as Maker fringes,[31] which arise when the second-harmonic light comes in and out of phase with the fundamental beam due to dispersion. We believe that the lack of Maker fringes (or indeed any appreciable change in the angle dependence with thickness) in the SHG from MEH-PPV films is due to the large absorption cross section of MEH-PPV at the 400 nm second-harmonic wavelength.[30,32,33]

Figure 2 shows the dependence of the SHG intensity on MEH-PPV film thickness; in this figure we took take advantage of the fact that the angle dependence of the SHG light does not change with thickness by integrating the angle-dependent data for each film (i.e., each point in Fig. 2 is the integral of a full angle-dependent SHG curve such as those shown in Fig. 1). The data show that the overall SHG intensity increases roughly linearly with film thickness, reaches a maximum at ~400 nm, and then decreases out to ~700 nm, the thickest MEH-PPV film we could produce by spin coating. Although the overall trend of the SHG intensity with film thickness appears robust, we note that in order to cover this large range of film thicknesses, we needed to cast films not just at many different spin speeds but also from solutions with three different concentrations.[34] The thickest films we studied were cast from a 1% w/v solution (blue circles), films of intermediate thickness were cast from a 0.5% w/v solution (green diamonds), and the thinnest films were cast from a 0.25% w/v solution (orange triangles). Careful inspection of Fig. 2 reveals that for the subset of films cast from each different solution, the SHG intensity first increases with thickness, reaches a maximum, and then decreases again for the thickest films.

To better understand the dependence of the SHG intensity for MEH-PPV films spin cast from different solutions, in Fig. 3(a), we show the same data in Fig. 2 plotted against spin speed (instead of overall film thickness) for each initial polymer solution concentration. This figure makes it clear that there is a self-similarity of the data with spin speed. In fact, when the overall thickness dependence is normalized
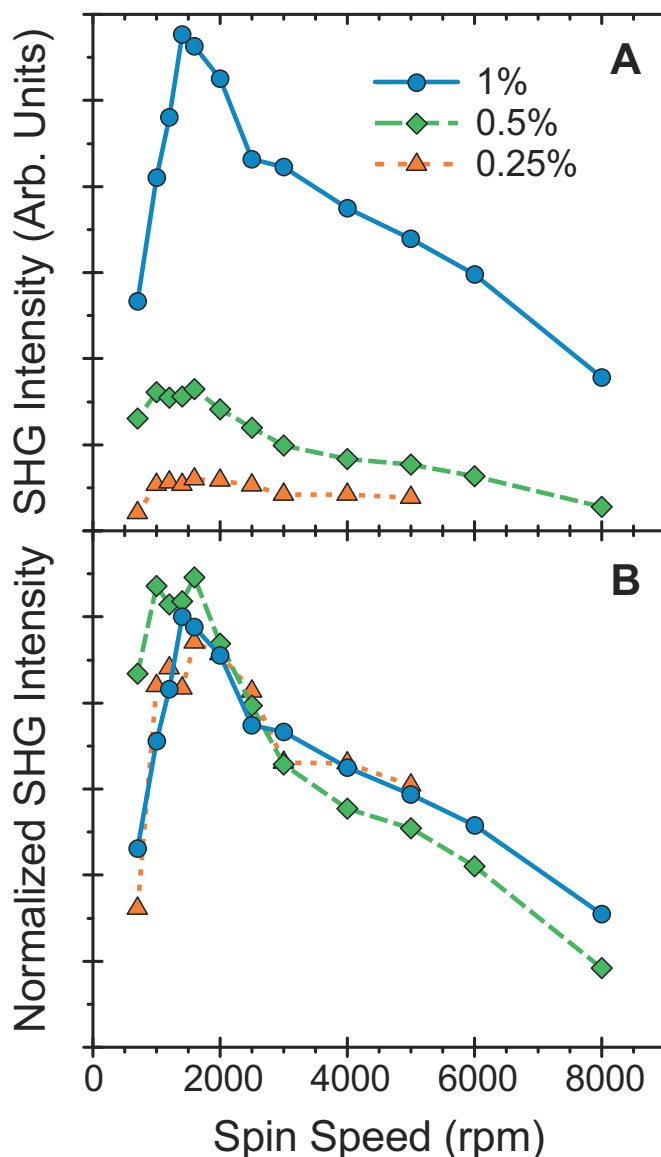
FIG. 3. (a) Angularly integrated SHG data for MEH-PPV films (same data and symbols as Fig. 2) plotted vs spin speed instead of film thickness. (b) The same data as in panel a, with the overall thickness dependence normalized out by scaling the data sets to minimize the squared deviations between them. It is clear that the SHG intensity has a similar trend with spin speed for films cast from different concentration solutions, with the SHG intensity reaching a maximum around 1400 rpm.

out, Fig. 3(b) shows that the trend of SHG intensity with spin speed is identical within error for all three solutions, indicating that a significant portion of the SHG signal is intrinsically dependent on the spin speed. What is perhaps even more surprising is that the trend is not monotonic: the SHG intensity is maximum for films spin cast around 1400 rpm, regardless of what solution concentration we used to cast the film.

Why should the SHG intensity from MEH-PPV films have such a pronounced dependence on spin speed? It is known that the bulk properties of MEH-PPV films depend on the speed with which the film was cast. For example, when spin casting films of MEH-PPV from the same solvent but from different solution concentrations and/or spin speeds, the peak of both the optical absorption and photoluminescence

spectra undergo slight shifts, which have been assigned to different degrees of aggregation of the conjugated chromophores.[35,36] These shifts are only observed for films made with solutions below the critical concentration, C*,[35] which is defined as the point at which the radius of gyration of the coiled polymer chains is equal to their mean center-of-mass separation distance (i.e., the point at which the polymer chains are on average in contact with their nearest neighbors). For films cast from solutions above this concentration, the linear optical properties no longer depend on the spin speed. Based on the optical absorbance spectra of our films, we know that the 1% w/v MEH-PPV solution is above C* and the other two solutions are below C* (see supporting information[27]), yet we see the same spin-speed trend in the SHG data in each set of films independent of the solution concentration. Thus, the underlying reasons for the changes in the linear and NLO properties of MEH-PPV films with spin-casting conditions must be different. To try to understand precisely what that difference might be, in Sec. III B, we use XRD to detail the way in which spin speed changes the physical morphology of the polymer chains in spin-cast MEH-PPV thin films.

B. The relationship between spin speed and local polymer crystallinity

One of the interesting features of conjugated polymer films is that their optical[35–51] and electrical[41,46,52,53] properties depend sensitively on the way in which the films were processed: casting from different solvents,[39,46,54–56] choosing different molecular weights[48,50,57] and different post-cast thermal[39,41,46,58–61] and solvent[62] treatments all can have dramatic effects on the electronic and optical properties of the resulting films. This is because the morphology of the polymer chains in a thin film depends on the processing conditions, and the optical and electrical properties are in turn sensitive to interactions between the polymer chromophores and thus to the morphology. When dissolved in good solvents, conjugated polymer chains become physically extended, and this extended chain conformation persists into the cast film, allowing the chromophores to couple through π-π interactions. Conversely, when conjugated polymer chains are dissolved in poor solvents, they coil tightly, limiting the degree of interchain coupling that carries over into the film.[44,46,53,54] Thus, many diverse properties of spin-cast films of conjugated polymers can be controlled by varying the processing conditions, creating a large parameter space to explore in order to optimize any particular subset of properties.

In order to determine precisely what structural properties of the MEH-PPV films might be responsible for the trends in SHG signal intensity with spin speed seen above, we performed grazing incidence XRD measurements on films that were spin cast from 1% w/v solutions. We integrated the 2D diffraction patterns along the in-plane (x), out-of-plane (z) and 45° axes in order to reveal the orientation of the aggregated MEH-PPV chains within any local crystalline domains. Figure 4 shows the packing structure of MEH-PPV crystalline domains, and Figure 5 shows representative XRD data
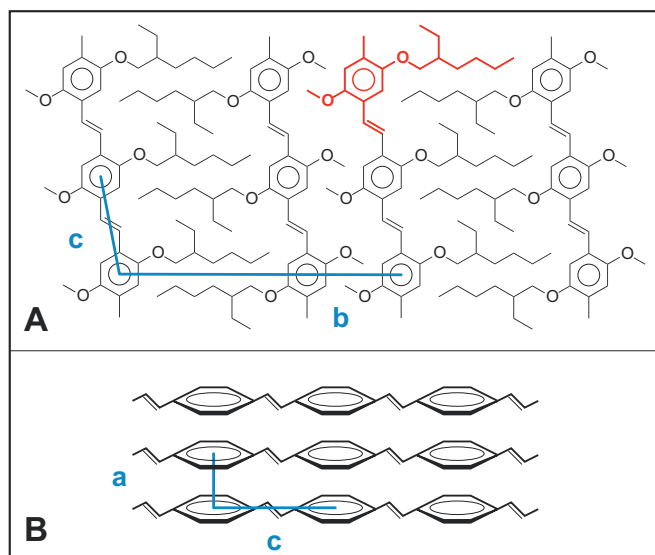
FIG. 4. Schematic model for the local packing of MEH-PPV chains looking down (a) the *a*-axis and (b) the *b*-axis. The characteristic lengths are represented by *a*, the interchain π-π stacking distance, *b*, the interchain spacing within a monolayer, and *c*, the monomer-to-monomer repeat unit spacing. In panel a, a single MEH-PPV monomer is highlighted in red. In panel b, the side chains have been omitted for clarity.
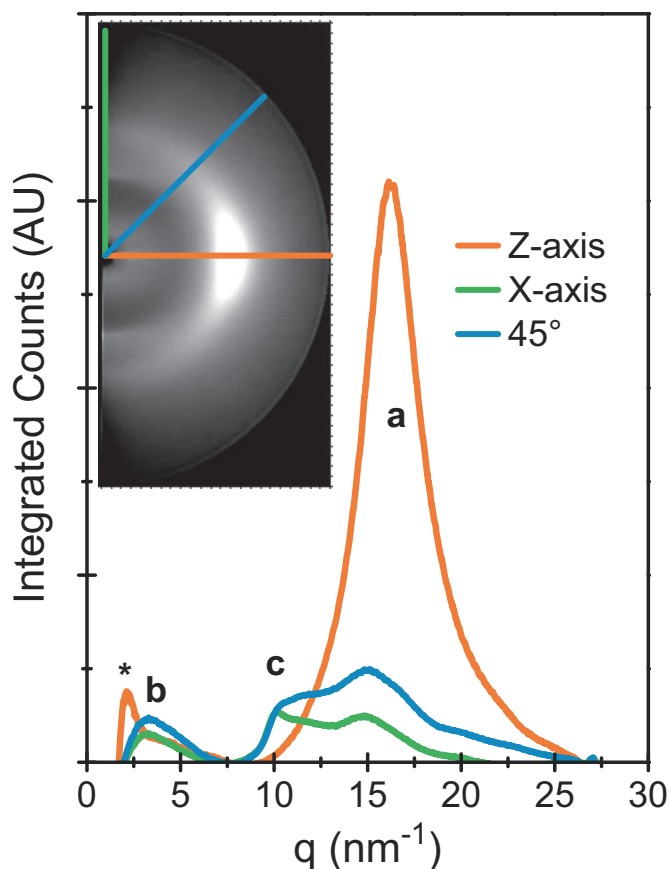

FIG. 5. 2D grazing incidence XRD of an MEH-PPV film spin-coated at 1400 rpm from a 1% w/v chlorobenzene solution. The inset shows the full two dimensional diffraction pattern, with cuts at various angles indicated by the colored lines. The *z*-axis is normal to the plane of the film, and the peaks labeled *a*, *b*, and *c* correspond to the crystallographic axes illustrated in Fig. 4. The peak marked with the asterisk is due to thin film reflection and is not a diffraction peak.

for a 435 nm thick film spin cast at 1400 rpm; for all of the MEH-PPV films, we observed three arcs in the diffraction patterns arising from the three primary crystallographic axes *a*, *b*, and *c* [Fig. 4].

The orange curve in Fig. 5 shows the *z*-axis integration of the full 2D diffraction pattern, revealing the structure of the MEH-PPV chains in the direction perpendicular to the substrate. The diffraction is dominated by a broad peak at scattering vector $q = 16.2$ nm^{-1}. This peak corresponds to the interchain backbone packing distance, marked *a* in Fig. 4(b), which has a value of 0.386 nm, consistent with previous observations for spin-coated MEH-PPV films.[61,63] The green curve in Fig. 5 shows the *x*-axis integration of the 2D diffraction, revealing two peaks that were not observed in the scattering along the *z*-axis. The peak at scattering vector $q = 10.15$ nm^{-1} corresponds to the monomer repeat distance of 0.628 nm, marked *c* in Fig. 4. The peak at $q = 2.54$ nm^{-1} corresponds to the *b* distance in Fig. 4(a); this in-plane distance between chains of 2.47 nm agrees well with previous diffraction studies, which indicate that the MEH-PPV ethylhexyloxy side groups are interdigitated.[61,63] The absence of these out-of-plane peaks in the *z*-axis integration in Fig. 5 indicates that the *c*- and *b*-axes of the MEH-PPV crystallites lie primarily in the plane of the film. The fact that these peaks are still observed when the 2D data is integrated at 45°, however, illustrates that the MEH-PPV chains are not rigorously oriented parallel to the substrate: indeed, all three angular integrations, 0°, 45°, and 90° show the peak corresponding to the crystallite *a*-axis, though the relative intensity of this peak varies with orientation.[61,63]

In order to determine the size and degree of orientational anisotropy of the MEH-PPV crystallites in our spin-cast films, we analyzed both the out-of-plane and in-plane diffraction peaks using the Scherrer equation.[64] The average widths of the diffraction peaks corresponding to the *a*, *b*, and

c lattice parameters are 4.2, 2.8, and 2.5 nm^{-1}, respectively. Using the width of the *a*-axis diffraction peak at $q = 16.25$ nm^{-1}, the Scherrer equation yields an average crystallite size of 1.8 nm. A similar analysis on the *c*-axis peak located at $q = 10.15$ nm^{-1} yields a crystallite size of 3.0 nm, while that for the *b*-axis peak yields a crystallite size of 2.7 nm. The fact that the widths of the peaks give different apparent crystallite sizes indicates that the crystallites are not spherical: the crystallites are instead anisotropic, extending along the *c*-axis for a distance of 5-6 polymer repeat units, but on the *a*-axis for only 4-5 repeat units and the *b*-axis for only 1-2 repeat units (or because each repeat unit consists of two polymer backbones with interdigitated 2-ethylhexoxy sidechains, 2-4 polymer chains, Fig. 4).

C. The relationship between spin speed and SHG in MEH-PPV thin films

Now that we understand the general morphology of MEH-PPV films, we turn our attention to how the morphology evolves as a function of spin speed. We found the best insight came when we considered the average degree of out-of-plane crystallinity of the spin-cast films, as measured by the integrated area of the *a*-axis scattering peak at $q = 16.25$ nm^{-1} in the *z* direction. Figure 6(a) correlates this
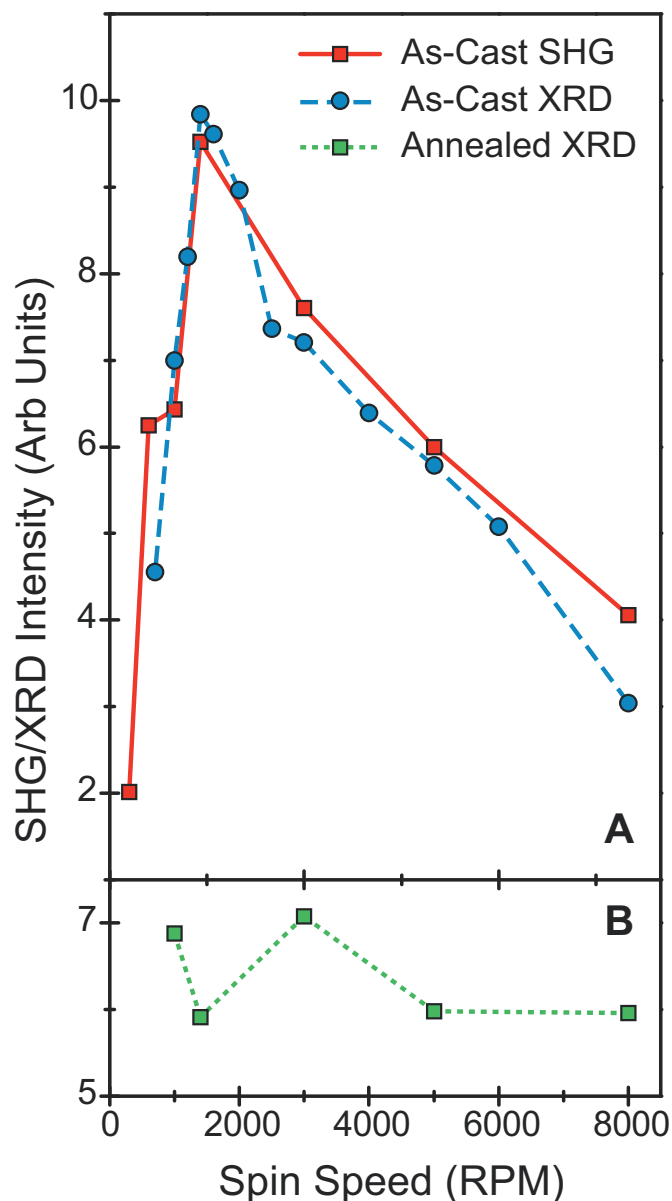
FIG. 6. (a) Integrated intensity of the *a*-axis XRD peak in the *z* direction (blue circles) and SHG intensity (red squares) for MEH-PPV films spin cast from 1% w/v chlorobenzene solutions as a function of spin speed. Because the ordinate for both data sets have arbitrary units, the SHG data was scaled to minimize the sum of the squared deviation between the two. The correlation between the degree of crystallinity as measured by the integrated diffraction and the SHG intensity is essentially perfect. (b) Integrated intensity of the *a*-axis XRD peak in the *z* direction (green squares) for annealed MEH-PPV films on the same vertical scale used in panel a. Upon annealing, the spin speed dependence of the crystallinity disappears.

measure of the degree of local crystallinity (blue circles) with the second-harmonic intensity (red squares; the same data shown in Fig. 3). In making this comparison, we have simply scaled the integrated SHG data to minimize the squared deviation between the two. The figure makes clear that the correlation between the SHG intensity and the degree of crystallinity is essentially perfect. The general spin speed trend in the XRD is observed not only for the out-of-plane peak corresponding to the crystallographic *a* axis, but also for the in-plane *a*-axis peak as well as for both the *b* and *c* peaks. Thus, the SHG intensity is providing information

about the degree of local crystallinity in the bulk of the film—it is not giving information that is specific to the interface(s). We will argue below that this is because the dipole approximation fails for MEH-PPV films, so that SHG is generated in the bulk via a quadrupole mechanism from the π-stacked chromophores.

Why should either the degree of MEH-PPV crystallinity or the SHG intensity depend so sensitively on the speed with which the film is spun? During the spin-coating process, there are two major physical effects that depend on the spin speed. First, the process of spin coating induces a net shear force on the individual polymer chains, which results from the balance between the centrifugal forces pulling outward and surface tension pulling inward. This shear force scales as the square of the rotational frequency,[34] and is likely what is responsible for the preferential alignment of the polymer chains parallel to the substrate. These forces also tend to stretch out the polymer chains, and one can anticipate that more stretched MEH-PPV chains will have a higher propensity for interchain interaction and π-π stacking. Second, the rate of solvent evaporation also depends on the spin speed. During spin coating, there is an area of solvent vapor immediately above the film through which solvent molecules in the film must diffuse through to escape. The thickness of this layer, and therefore the diffusion rate, is proportional to the inverse square of the rotational frequency.[34] The less time it takes for the solvent to evaporate, the more likely the polymer chains will be kinetically trapped in a structure far from their local energetic minimum.

For spin-cast MEH-PPV films, the shear forces are relatively small at spin speeds below 1400 rpm, but the solvent can take as long as 10 min (at 300 rpm) to evaporate to the point that the film can be removed from the spin-coater. In this low-spin-speed limit, the polymer chains have plenty of time to relax, but because the shear forces are small and the solvent/polymer interaction dominates, the polymer chains tends to retain their coiled solution configuration. At high spin speeds, on the other hand, the shear forces are large but the solvent evaporates so quickly (less than 10 s at 8000 rpm) that the chains become kinetically locked into their coiled solvent configuration before they can untangle. Evidently, the balance between these two extremes occurs near 1400 rpm: the MEH-PPV remains dissolved long enough and the shear forces are large enough to stretch the chains, increasing the degree of π-π interaction and thus the extent of local crystallinity. Since interactions between conjugated polymer chains result in a significant interchain electronic polarizability, it is perhaps not surprising that the SHG intensity is sensitive to this polarizability, particularly if the SHG results from a bulk quadrupolar interaction.[65]

D. The effects of thermal annealing on MEH-PPV structure and SHG

In addition to varying the spin speed and solution concentration, another common method of processing conjugated polymer films for optoelectronic applications is thermal annealing.[39,41,46,58–61] In thermal annealing, spin-cast films are heated above the conjugated polymer's glass transition temperature, so that the chains become mobile and can
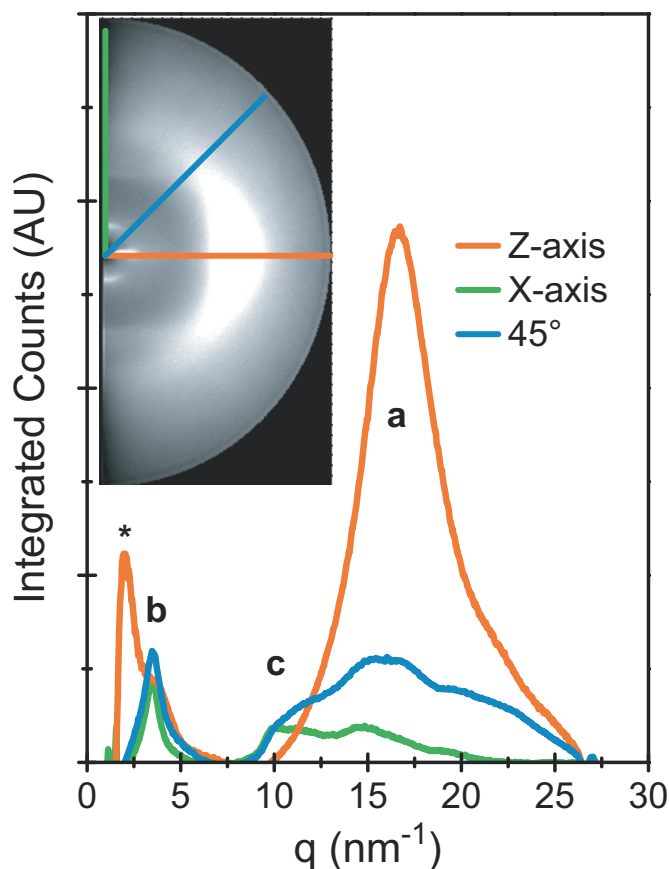
FIG. 7. 2D grazing incidence XRD of an MEH-PPV film prepared identically to that studied in Fig. 5 but following thermal annealing at 210 °C for 12 h. The inset shows the full 2D scattering pattern, and the colored curves show cuts in different directions (same as in Fig. 5). The peak marked with an asterisk is due to thin film reflection and is not a diffraction peak.

relax from the structure in which they were originally kinetically trapped from the spin-coating process. Indeed, previous work has noted that thermal annealing appears to erase all the spin-coating dependent processing history of MEH-PPV thin films.[39,41] In this section, we use XRD to quantify the structural changes that take place in MEH-PPV films following thermal annealing. We then use the fact that annealing produces films with the same degree of local MEH-PPV crystallinity to examine how the SHG intensity varies with the film thickness at a constant degree of crystallinity.

1. How thermal annealing changes the crystallinity of MEH-PPV films

Figure 7 shows the 2D grazing-incidence XRD from an MEH-PPV film that was initially prepared under identical conditions to the one whose XRD pattern is shown in Fig. 5, but was subsequently thermally annealed for 12 h at 210 °C. A comparison of Figs. 5 and 7 shows that even when starting from the most crystalline MEH-PPV film that can be prepared via spin coating, thermal annealing still causes additional changes to the film's physical structure. The most obvious change is the fact that the large peak corresponding to the a spacing shifts from $q = 16.2$ nm^{-1} in the as-cast film to $q = 16.6$ nm^{-1} in the annealed film. This shift indicates that the thermal annealing decreases the average distance between the polymer chains; the annealing process allows the

chains to adopt a more thermodynamically stable tight-packed configuration. The peak at $q = 10.15$ nm^{-1} remains unchanged upon thermal annealing, as would be expected for diffraction that corresponds to the spacing between the monomer units along the polymer backbone. Finally, the largest change induced by thermal annealing occurs with the peak that corresponds to the b spacing, which shifts from 2.54 nm^{-1} in the as-cast film to 3.46 nm^{-1} after annealing. This means thermal annealing decreases the b spacing to 1.81 nm, a distance that is simply too small to be consistent with the simple interdigitated side-chain structure of the as-cast films shown in Fig. 4(a). It has been previously proposed[61] that this shift to a lower b-spacing upon thermal annealing is achieved through an out-of-plane tilt of the interdigitated alkyl side chains.

In addition to the changes in the local crystal structure, the data in Fig. 7 show that thermal annealing also changes both the average orientation of the MEH-PPV chains and the size of the crystallites. The fact that the annealed films show a higher out-of-plane:in-plane peak intensity ratio than any of the as-cast films indicates that the annealing process induces additional preferential ordering of the nanocrystalline domains parallel to the substrate. In addition, when we use the Scherrer equation to estimate the average size of the nanocrystalline domains in the annealed films, we obtain values of 1.5, 6.8, and 3.0 nm for the peaks corresponding to the a-, b- and c-axes, respectively. Thus, thermal annealing causes the domain size to increase in the b direction, and to decrease slightly in the a direction. But most importantly, we see in Fig. 6(b) that the degree of out-of-plane crystallinity is independent of spin speed after thermal annealing, in agreement with other studies that show that thermal annealing erases the effect of casting conditions.[39,41]

2. The thickness dependence of the SHG intensity from annealed MEH-PPV films

Attempting to model the way in which the second-harmonic light intensity changes with the thickness of as-cast MEH-PPV films is a difficult task because each film has a different degree of crystallinity, and therefore a different value for the effective second-order susceptibility. However, with the XRD data in Fig. 6(b) that shows that thermal annealing erases any spin-speed-dependent differences in MEH-PPV film crystallinity, we can examine how the SHG intensity changes with thickness in annealed MEH-PPV films. Figure 8 shows the integrated SHG signal from annealed MEH-PPV films as a function of thickness. Here, unlike in Fig. 2, the SHG from the films cast from the three concentration regimes neatly overlap one another, steadily increasing with thickness to a maximum around 450 nm. This verifies that, as suggested by the XRD data discussed above, there is no longer any spin-speed dependent component to the intensity of the SHG from thermally annealed MEH-PPV films.

To model the dependence of the SHG data on annealed film thickness, we start with the fact that SHG is characterized by the second-order induced polarization in a material[66]
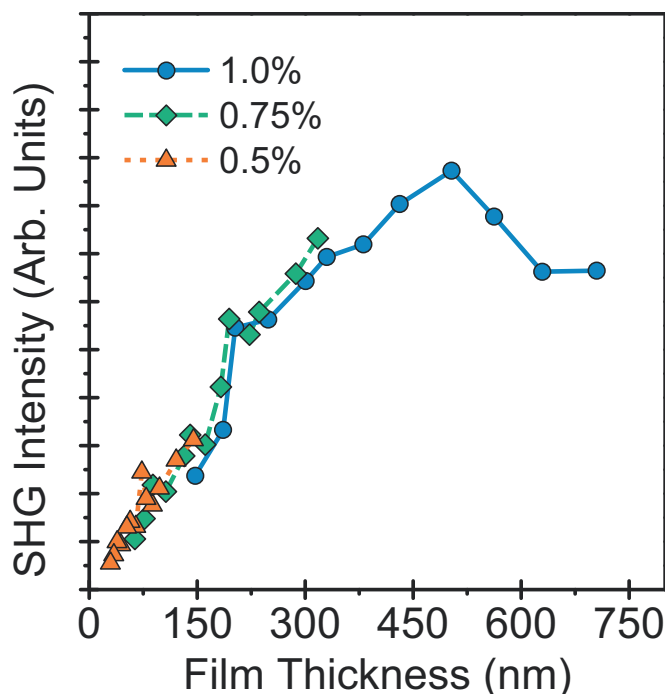
FIG. 8. Integrated SHG for annealed films cast from three different solution concentrations shown on a linear-linear plot. Unlike the case with unannealed films (cf. Fig. 2), the SHG signal from the films made from the three different solution concentrations completely overlap, verifying that there is no longer a spin-speed dependent component to the signal.

$$P_i^{(2)} = \chi_{ijk}^{(2)} E_j E_k + G_{ijkl}^{(2)} E_j \partial_k E_l, \tag{1}$$

where each of the indices range over the Cartesian coordinates x, y, and z, and repeated indices are summed. The first term on the right-hand side of Eq. (1) is the often-used electric dipole (ED) term, where $\boldsymbol{\chi}^{(2)}$ is the second-order susceptibility, a 27-element rank 3 tensor that connects the components of the two incident electric fields, $\vec{E}$, to the induced polarization, $\boldsymbol{P}^{(2)}$. Once $\boldsymbol{P}^{(2)}$ is determined, the detected output field can be determined by using it as the source term in Maxwell's wave equation.[67] The unique nonzero elements of $\boldsymbol{\chi}^{(2)}$ are determined by the space-group symmetry of the material. In centrosymmetric materials, all the elements of $\boldsymbol{\chi}^{(2)}$ are zero. At an interface where the center of symmetry is broken ($C_{\infty v}$ symmetry), however, $\boldsymbol{\chi}^{(2)}$ has seven nonzero elements, three of which are unique.[19] The second term on the right-hand side of Eq. (1) is the next higher-order in the expansion of the polarization in the electric field, which relates the polarization to the electric field and its gradient through $\boldsymbol{G}^{(2)}$, an 81-element, rank 4 tensor that can be decomposed into electric quadrupole (EQ), magnetic dipole (MD), ED/EQ coupling, and ED/MD coupling.[68] Because these high-order contributions belong to different symmetry classes than ED, they do not vanish in centrosymmetric media.[66]

The fact that the SHG intensity from unannealed MEH-PPV films correlates so strongly with the degree of bulk crystallinity measured by XRD [Fig. 6(a)] strongly suggests that we need to consider high-order effects that allow for second harmonic to be generated in the bulk. This idea of SHG arising from the bulk of MEH-PPV films is not unprec-

edented, as bulk SHG from terms higher-order than the ED approximation has been identified in films of at least two other centrosymmetric organic systems with high degrees of π-conjugation: buckminsterfullerene (C_{60}) (Ref. 69) and metal phthalocyanines.[70] For thermally evaporated thin films of C_{60}, a large thickness-dependent SHG response was determined to be dominated by MD terms by examining the symmetry of $\boldsymbol{G}^{(2)}$ in a phase-sensitive SHG experiment.[69] For thermally evaporated metal phthalocyanine films on glass, fits of the bulk SHG intensity as a function of film thickness suggested that the EQ mechanism was primarily responsible for the NLO response of the films.[66,70]

Because the data in Fig. 8 are similar to that observed in the previous work on metal phthalocyanines,[66,70] we have elected to model our SHG data from annealed MEH-PPV films using the same approach. As a start for our model, we used literature values of the refractive index of MEH-PPV (Ref. 30) to determine the necessary Fresnel coefficients. We then followed the procedure of Hoshi *et al.* in fitting the full angle- and thickness-dependent SHG intensity from the annealed MEH-PPV films to the different possible mechanisms for interfacial and bulk SHG;[66] details are given in the supporting information.[27] Figure 9(b) shows the full SHG data set for our annealed MEH-PPV films; panels a and c in this figure show the results for the best ED and EQ fits to the data, respectively. The bottom panels in this figure show cuts of the full data (data points connected by lines) and both fits (red curves) for representative slices at constant angle (52°, the angle of maximum signal) and constant thickness (317 nm, near the center of the thickness range). The figure makes clear that the EQ mechanism fits the full SHG data set better than the ED mechanism: the ED mechanism cannot adequately reproduce the shape of the thickness-dependent SHG data from annealed MEH-PPV films, and the ED mechanism provides a poorer fit for the angle-dependent SHG than the EQ mechanism. This suggests that like C_{60} and metal phthalocyanines, the SHG from conjugated polymer films comes primarily from the bulk. Moreover, the data on the as-cast MEH-PPV films presented above suggests that the polarizability depends sensitively on the degree of chromophore interactions, which in turn depends on the degree of bulk crystallinity in the film. Thus, SHG is not a technique that can examine conjugated polymer interfaces, but it can provide detailed information about the microcrystallinity of the conjugated chromophores in the bulk of the film.

The fact that second-order NLO signals in conjugated polymer films are generated from the bulk rather than the interface has important implications for previous studies. Li *et al.*[22] have claimed to measure interfacial electronic states of MEH-PPV films by performing doubly resonance enhanced sum-frequency generation (DR-SFG). SFG works much the same as SHG, except that the two electric fields in Eq. (1) are no longer degenerate. In conventional SFG, a nonresonant visible field is held fixed and an IR field is scanned over a range of frequencies, so that the output polarization is resonance enhanced and the vibrational states at the interface can be mapped out. In DR-SFG, both the visible and IR fields are scanned, allowing the coupling between the electronic and vibrational states to be measured.[71] Li *et al.*
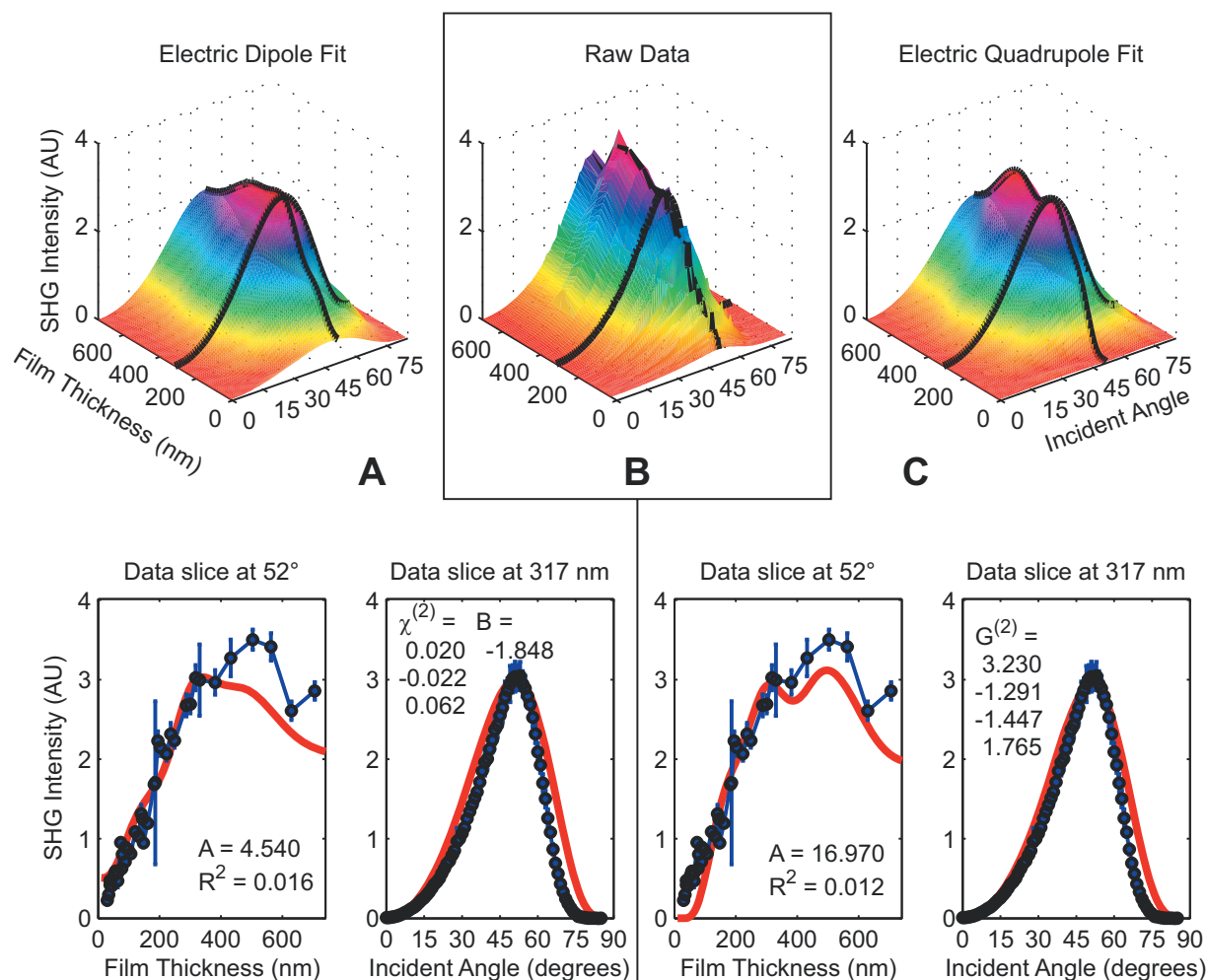
FIG. 9. Comparison of ED and EQ SHG models for annealed MEH-PPV films. Along the top, from left to right, are the full 3D model fit for the ED model (panel a), the raw SHG data (panel b), and the model fit for the EQ model (panel c). Black lines indicate the location of the slices in the lower plots of panels a and c. The ED fits in panel a do a better job of fitting the data at smaller thicknesses, but do poorly for large thicknesses; the EQ fits in panel b do a better overall job of fitting the data, particularly at larger thicknesses.

used DR-SFG to measure the electronic states associated with the C–C stretch of the benzene ring in the MEH-PPV backbone. Their interpretation of the resulting electronic spectrum as being that at the MEH-PPV interface, however, presumes that the ED approximation holds and that the second-order NLO signals are generated entirely from the interface. Instead, the results presented above suggest that the ED approximation fails and that the second-order NLO signals in conjugated polymer films arise primarily from the bulk. This means that the DR-SFG experiment was more likely measuring something akin to the bulk resonance Raman excitation profile of the benzene C–C stretch and not any type of interfacial electronic structure. It would be interesting to compare the results of Ref. 22 to resonance Raman excitation studies of MEH-PPV films to further determine whether or not any type of second-order NLO process can provide interface-specific information regarding conjugated polymer films.

IV. CONCLUSIONS

In this work, we originally set out to use NLO techniques to understand interfaces in spin-coated thin films of

conjugated polymers such as MEH-PPV. Instead, we discovered that the SHG from MEH-PPV films is dominated by the symmetry-allowed EQ response from the bulk. One manifestation of this is that the bulk SHG signal resonant with the lowest energy absorption peak depends strongly on the spin speed used during the film spin-coating process. This spin-speed dependence to the SHG signal is independent of the concentration of the solution used to cast the films and follows a different trend than that observed in linear optical measurements. Using 2D XRD, we saw that the total number of π-stacked crystalline polymer domains aligned parallel to the plane of the film followed the exact same trend with spin speed as the SHG intensity. In particular, the maximum SHG signal and film crystallinity both occur at a spin speed of 1400 rpm and fall off in an identical fashion at both faster and slower spin speeds. Thus, a significant part of the SHG signal from MEH-PPV films must arise from these bulk crystalline domains and not from the polymer interfaces.

We propose that the nonmonotonic spin-speed dependence of both the polymer crystallinity and the SHG intensity is due to a competition between the shear forces present during spin coating, which favor greater π-π interaction by

stretching out the chains, and the solvent evaporation rate, which kinetically traps the polymer chains in their coiled solvent configuration at higher speeds. Low spin speeds provide little shear force to stretch out the polymer chains, leading to low overall crystallinity. The large shear forces at high spin speeds, on the other hand, do not act long enough to stretch the chains, again resulting in low crystallinity. Thus, the greatest amount of crystallinity occurs at intermediate spin speeds.

The idea that the SHG intensity correlates with the degree of film crystallinity is perhaps not that surprising. It is well known that the electronic states of conjugated polymers can delocalize when the chains have a good degree of π-electron contact, thus increasing the polarizability of the material and the second-order NLO response. The fact that these delocalized π-electrons can give rise to bulk SHG is consistent with observations from other π-stacked organic systems, most notably phthalocyanine dyes, which exhibit similar bulk SHG arising from an EQ moment.

Finally, we were able to verify the bulk quadrupole mechanism of the SHG from MEH-PPV films by taking advantage of the fact that thermal annealing can erase any differences in the processing-history dependent film morphology. Using XRD, we showed that thermally annealed MEH-PPV films of different thickness had the same degree of crystallinity, allowing us to model the overall thickness and angle dependence of the SHG with a single NLO polarizability tensor. We found that the SHG from MEH-PPV films is indeed best modeled with a bulk-allowed EQ mechanism. This opens up the possibility of using SHG as a tool to rapidly assess the degree of crystallinity of conjugated polymer films *in situ* without having to resort to more complex experiments such as XRD.

ACKNOWLEDGMENTS

[1] I. Samuel and G. Turnbull, Chem. Rev. (Washington, D.C.) **107**, 1272 (2007).
[2] H. Sirringhaus, Adv. Mater. (Weinheim, Ger.) **17**, 2411 (2005).
[3] J.-M. Nunzi, C. R. Phys. **3**, 523 (2002).
[4] D. T. McQuade, A. E. Pullen, and T. M. Swager, Chem. Rev. (Washington, D.C.) **100**, 2537 (2000).
[5] M. Jaiswal and R. Menon, Polym. Int. **55**, 1371 (2006).
[6] H. E. Katz and J. Huang, Annu. Rev. Mater. Res. **39**, 71 (2009).
[7] N. Ide, H. Tsuji, N. Ito, H. Sasaki, T. Nishimori, Y. Kuzuoka, K. Fujihara, T. Miyai, and T. Komoda, in *Organic Light Emitting Materials and Devices XII*, The International Society for Optical Engineering Vol. 7051, edited by F. So and C. Adachi (SPIE, San Diego, CA, 2008), p. 705119.
[8] V. van Elsbergen, H. Boerner, H.-P. Löbl, C. Goldmann, S. P. Grabowski, E. Young, G. Gaertner, and H. Greiner, in *Organic Light Emitting Materials and Devices XII*, The International Society for Optical Engineering Vol. 7051, edited by F. So and C. Adachi, (SPIE, San Diego, CA, 2008), p. 70511A.
[9] F. C. Krebs, Sol. Energy Mater. Sol. Cells **93**, 394 (2009).
[10] J. Liu, T. F. Guo, Y. J. Shi, and Y. Yang, J. Appl. Phys. **89**, 3668 (2001).
[11] W. Salaneck, J. Electron Spectrosc. Relat. Phenom. **174**, 3 (2009).
[12] A. Kahn, N. Koch, and W. Gao, J. Polym. Sci., Part B: Polym. Phys. **41**, 2529 (2003).
[13] S. Li, E. T. Kang, Z. H. Ma, and K. L. Tan, Surf. Interface Anal. **29**, 95 (2000).
[14] M. Atreya, S. Li, E. T. Kang, K. G. Neoh, Z. H. Ma, and K. L. Tan, J. Vac. Sci. Technol. A **17**, 853 (1999).
[15] H. Li, D. R. Powell, R. K. Hayashi, and R. West, Macromolecules **31**, 52 (1998).
[16] Y. R. Shen, Annu. Rev. Phys. Chem. **40**, 327 (1989).
[17] Z. Chen, Y. R. Shen, and G. A. Somorjai, Annu. Rev. Phys. Chem. **53**, 437 (2002).
[18] Y.-R. Shen, *The Principles Of Nonlinear Optics* (Wiley-Interscience, Hoboken, NJ, 2003).
[19] R. W. Boyd, *Nonlinear Optics*, 2nd ed. (Academic, New York, 2002).
[20] P. N. Butcher and D. Cotter, *The Elements of Nonlinear Optics, Cambridge Studies in Modern Optics* (Cambridge University Press, Cambridge, UK, 1991), Vol. 9.
[21] R. Hildebrandt, H. M. Keller, G. Marowsky, W. Brutting, T. Fehn, M. Schwoerer, and J. E. Sipe, Chem. Phys. **245**, 341 (1999).
[22] Q. Li and K. C. Chou, Proc. SPIE **7396**, 73960Q (2009).
[23] F. Wudl and G. Srdanov, U.S. Patent No. 5,189,136 (23 February 1993).
[24] C. J. Neef and J. P. Ferraris, Macromolecules **33**, 2311 (2000).
[25] C. J. Neef and J. P. Ferraris, Macromolecules **37**, 2671 (2004).
[26] J. P. Ferraris, private communication (2002).
[27] See supplementary material at http://dx.doi.org/10.1063/1.3436517 for details of MEH-PPV synthesis, SHG experimental setup, and data modeling details.
[28] T.-Q. Nguyen and B. J. Schwartz, J. Chem. Phys. **116**, 8198 (2002).
[29] S. J. Martin, H. Mellor, D. D. C. Bradley, and P. L. Burn, Opt. Mater. **9**, 88 (1998).
[30] M. Tammer and A. P. Monkman, Adv. Mater. (Weinheim, Ger.) **14**, 210 (2002).
[31] P. D. Maker, R. W. Terhune, M. Nisenoff, and C. M. Savage, Phys. Rev. Lett. **8**, 21 (1962).
[32] W. N. Herman and L. M. Hayden, J. Opt. Soc. Am. B **12**, 416 (1995).
[33] B. Berge, A. Wicker, J. Lajzerowicz, and J. F. Legrand, Europhys. Lett. **9**, 657 (1989).
[34] D. E. Haas, J. N. Quijada, S. J. Picone, and D. P. Birnie III, Proc. SPIE **3943**, 280 (2000).
[35] Y. Shi, J. Liu, and Y. Yang, J. Appl. Phys. **87**, 4254 (2000).
[36] Y. Shi, J. Liu, and Y. Yang, Macromol. Symp. **154**, 187 (2000).
[37] T. W. Hagler, K. Pakbaz, and A. J. Heeger, Phys. Rev. B **49**, 10968 (1994).
[38] R. Chang, J. H. Hsu, W. S. Fann, K. K. Liang, C. H. Chiang, M. Hayashi, J. Yu, S. H. Lin, E. C. Chang, K. R. Chuang, and S. A. Chen, Chem. Phys. Lett. **317**, 142 (2000).
[39] T.-Q. Nguyen, I. B. Martini, J. Liu, and B. J. Schwartz, J. Phys. Chem. B **104**, 237 (2000).
[40] T. Q. Nguyen, J. J. Wu, V. Doan, B. J. Schwartz, and S. H. Tolbert, Science **288**, 652 (2000).
[41] T. W. Lee and O. O. Park, Appl. Phys. Lett. **77**, 3334 (2000).
[42] T. Q. Nguyen, J. Wu, S. H. Tolbert, and B. J. Schwartz, Adv. Mater. (Weinheim, Ger.) **13**, 609 (2001).
[43] S. H. Tolbert, J. J. Wu, A. F. Gross, T. Q. Nguyen, and B. J. Schwartz, Microporous Mesoporous Mater. **44–45**, 445 (2001).
[44] C. J. Collison, L. J. Rothberg, V. Treemaneekarn, and Y. Li, Macromolecules **34**, 2346 (2001).
[45] J. H. Hsu, M. T. Hayashi, S. H. Lin, W. S. Fann, L. J. Rothberg, G. Y. Perng, and S. A. Chen, J. Phys. Chem. B **106**, 8582 (2002).
[46] B. J. Schwartz, Annu. Rev. Phys. Chem. **54**, 141 (2003).
[47] W. C. Molenkamp, M. Watanabe, H. Miyata, and S. H. Tolbert, J. Am. Chem. Soc. **126**, 4476 (2004).
[48] K. Koynov, A. Bahtiar, T. Ahn, C. Bubeck, and H. H. Horhold, Appl. Phys. Lett. **84**, 3792 (2004).
[49] A. J. Cadby and S. H. Tolbert, J. Phys. Chem. B **109**, 17879 (2005).
[50] K. Koynov, A. Bahtiar, T. Ahn, R. M. Cordeiro, H. H. Horhold, and C. Bubeck, Macromolecules **39**, 8692 (2006).
[51] I. B. Martini, I. M. Craig, W. C. Molenkamp, H. Miyata, S. H. Tolbert, and B. J. Schwartz, Nat. Nanotechnol. **2**, 647 (2007).
[52] M. G. Harrison, J. Gruner, and G. C. W. Spencer, Phys. Rev. B **55**, 7831

(1997).

[53] T. Q. Nguyen, R. C. Kwong, M. E. Thompson, and B. J. Schwartz, Synth. Met. **119**, 523 (2001).

[54] T.-Q. Nguyen, V. Doan, and B. J. Schwartz, J. Chem. Phys. **110**, 4068 (1999).

[55] T. Q. Nguyen, R. Y. Yee, and B. J. Schwartz, J. Photochem. Photobiol., A **144**, 21 (2001).

[56] W. Holzer, A. Penzkofer, H. Tillmann, and H. H. Horhold, Synth. Met. **140**, 155 (2004).

[57] A. Bahtiar, K. Koynov, T. Ahn, and C. Bubeck, J. Phys. Chem. B **112**, 3605 (2008).

[58] T. Q. Nguyen, R. C. Kwong, M. E. Thompson, and B. J. Schwartz, Appl. Phys. Lett. **76**, 2454 (2000).

[59] T. Q. Nguyen, B. J. Schwartz, R. D. Schaller, J. C. Johnson, L. F. Lee, L. H. Haber, and R. J. Saykally, J. Phys. Chem. B **105**, 5153 (2001).

[60] R. D. Schaller, P. T. Snee, J. C. Johnson, L. F. Lee, K. R. Wilson, L. H. Haber, R. J. Saykally, T.-Q. Nguyen, and B. J. Schwartz, J. Chem. Phys. **117**, 6688 (2002).

[61] U. Jeng, C.-H. Hsu, H.-S. Sheu, H.-Y. Lee, A. Inigo, H. Chiu, W. Fann, S. Chen, A. Su, T.-L. Lin, K. Peng, and S. Chen, Macromolecules **38**, 6566 (2005).

[62] G. Li, Y. Yao, H. Yang, V. Shrotriya, G. Yang, and Y. Yang, Adv. Funct. Mater. **17**, 1636 (2007).

[63] Y.-F. Huang, C.-W. Chang, D.-M. Smilgies, U.-S. Jeng, A. R. Inigo, J. D. White, K.-C. Li, T.-S. Lim, T.-D. Li, H.-Y. Chen, S.-A. Chen, W.-C. Chen, and W.-S. Fann, Adv. Mater. (Weinheim, Ger.) **21**, 2988 (2009).

[64] B. Cullity and S. Stock, *Elements of X-Ray Diffraction*, 3rd ed. (Prentice-Hall, Englewood Cliffs, NJ, 2001).

[65] M. Sato, A. Takeuchi, T. Yamada, H. Hoshi, K. Ishikawa, T. Mori, and H. Takezoe, Phys. Rev. E **56**, R6264 (1997).

[66] H. Hoshi, T. Yamada, K. Ishikawa, H. Takezoe, and A. Fukuda, Phys. Rev. B **52**, 12355 (1995).

[67] J. D. Jackson, *Classical Electrodynamics*, 3rd ed. (Wiley, New York, 1998).

[68] E. Adler, Phys. Rev. **134**, A728 (1964).

[69] B. Koopmans, A. M. Janner, H. T. Jonkman, G. A. Sawatzky, and F. Vanderwoude, Phys. Rev. Lett. **71**, 3569 (1993).

[70] T. Yamada, H. Hoshi, K. Ishikawa, H. Takezoe, and A. Fukuda, Jpn. J. Appl. Phys., Part 2 **34**, L299 (1995).

[71] M. B. Raschke, M. Hayashi, S. H. Lin, and Y. R. Shen, Chem. Phys. Lett. **359**, 367 (2002).